R. Andreotti, M. Colombo, A. Guardone, P. Martinelli, G. Riganti, M. Di Prisco
Performance of a Shock Tube Facility for Impact Response of Structures
International Journal of Non-Linear Mechanics, Vol. 72, 2015, p. 53-66
doi:10.1016/j.ijnonlinmec.2015.02.010

Performance of a shock tube facility for impact response of structures

Riccardo Andreotti[1], Matteo Colombo[2], Alberto Guardone[3], Paolo Martinelli[4*], Gianmario Riganti[5] and Marco di Prisco[6]

[1] Director of mechanical systems analysis and numerical modeling, AREA3 Calculation Center, Via Raffaello 6, 21022 Azzate VA (Italy) and Adjunct Lecturer, Department of Mechanical Engineering, Politecnico di Milano, via La Masa 1, 20156 - Milano (Italy).
[2] Assistant Professor, Department of Civil and Environmental Engineering, Politecnico di Milano, P.za L. da Vinci 32, 20133 Milano (Italy)
[3] Associate Professor, Department of Aerospace Science and Technology, Politecnico di Milano, via La Masa 34, 20156 - Milano (Italy)
[4*] Corresponding author, Assistant Professor, Department of Civil and Environmental Engineering, Politecnico di Milano, P.za L. da Vinci 32, 20133 Milano (Italy)
e-mail:paolo.martinelli@polimi.it ; tel: +39 02 2399 8785; fax: +39 02 2399 8771
[5] Research Associate, Department of Environment, Constructions and Design, University of Applied Sciences of Southern Switzerland, Lugano, (Switzerland).
[6] Full Professor, Department of Civil and Environmental Engineering, Politecnico di Milano, P.za L. da Vinci 32, 20133 Milano (Italy)

ABSTRACT

This paper presents a numerical approach to compute the performance of a double diaphragm shock tube facility for structural response investigations. To assess the influence of different sources of dissipation, including partial diaphragm opening and shock tube vibration, numerical simulations are carried out using several different finite element models of increasing complexity to compute shock tube performance. The numerical model accounting for tearing and partial opening of the diaphragms is the one that best reproduces the results of the experiment, thus indicating that the diaphragm non-ideal opening process is the most relevant cause of losses. Both the numerical and the experimental results agree in predicting shock tube efficiency in terms of intensity of the reflected shock of about 50-60% with respect to ideal, one-dimensional conditions.

Keywords: shock tube performance, shock tube for structural testing, finite-element scheme, finite-volume scheme, fluid-structure interaction.

1 INTRODUCTION

The response of critical civil and industrial infrastructure such as government structures, nuclear power plants, power stations, tunnels and shopping centers to shock and blast loading has become a topic of great interest. Terrorist attacks around the world and the resulting casualties and damage have highlighted the vulnerability of existing infrastructure to the highly impulsive nature of the blast loads. It is primarily government and military organizations that have developed blast resistant design guidelines and retrofit procedures, while the civil engineering community has not traditionally been involved in blast engineering research. The methods currently adopted in blast-resistant design are largely based on empirical observations of live explosive tests [1-11].

Experimental activities are particularly relevant in this field not only for validating computational methods, but also because of the limited amount of existing experimental blast data. Experimental investigation of structures or structural components has traditionally been performed through live explosive testing, but the use of explosives remains very limited due to its dangerous and expensive nature. An alternative technique for creating impulse loading on portions of a structure involves use of shock tubes; they offer an opportunity to impose on the specimen surface the loading history typical of blast waves due to explosions. As reported, for example, in [12], the use of shock tubes to create impulsive loading scenarios has several advantages over the use of explosives, such as safety, cost and repeatability of experiments, though it also has some limitations, mainly related to the size of the structural members tested.

There has been considerable interest in research into blast simulation methods since the 1960s, at which time a research symposium titled "Military Applications of Blast Simulation" was formed for the sole purpose of designing blast simulators to produce the specially tailored waveforms representative of nuclear blasts [13-14]. By the mid-1980s, with the aim of measuring blast loads from nuclear explosions on full-sized military equipment such as tanks, small aircraft and helicopters, several large air-blast simulators had been built in various countries as part of a well-financed defense effort as, for example, the facility described in [15]. The use of shock tubes to simulate blast loading on structures is not new, and this technique was developed to reproduce blast waves nearly identical to those obtained in live explosive tests [16-17]. The literature reports experimental observations for material blast testing covering concrete specimens [18-19], steel plates [20], reinforced masonry walls [21] and polymeric materials [22]. In recent years, new shock tube facilities have been developed for structural applications [12, 23-25] and the response of composite materials, including glass-reinforced polymers, 3-D woven composites [23, 26] and fiber-reinforced concrete materials [27], has been investigated.

The importance of shock tube facilities in blast engineering is thus apparent. However, this growing interest in shock tube development has not been matched by studies of shock tube efficiency. In fact, the design of a shock tube facility for blast engineering applications involves many challenges, mainly due to the difficulty of predicting the pressure history against the specimen, which, together with the impulse and the duration of the positive phase, is the most important parameter in order to correctly load the specimen.

Pressure loads are strongly influenced by several parameters, such as tube geometry (boundary layer effect), tube wall response and the diaphragm opening process. Note that the diaphragm opening process is difficult to assess using an analytical approach. Previous studies have investigated tube wall deformation when subjected to internal shock waves [28-33], the mutual interaction between the shock wave and the structure [34-35], the boundary layer effect on the shock wave [36-40] and the influence of incomplete diaphragm opening on shock wave formation [41-46], including the structural dynamics and the diaphragm failure mechanism [47-48].

This paper presents a numerical approach based on finite element (FE) models used to predict the performance of a facility recently developed in Italy [25]. The efficiency of the device is evaluated taking several sources of dissipation into account. Due to the fact that the shock tube under study is intended for structural applications, shock tube performance is evaluated here in terms of the peak value of the pressure at the end-wall position. In the following, with a slight misuse of technical terms, we refer to the reflection of the impinging shock wave as “reflected pressure”, to distinguish it from the “incident pressure” measured before the arrival of the shock wave, in accordance with standard practice in describing shock tube flows for blast engineering.

This paper is intended to provide guidelines to researchers for designing effective shock-tube facilities for structural engineering applications. The authors wish to share the methods they devised in order to verify the experimental apparatus developed at the Politecnico di Milano.

2 EXPERIMENTAL APPARATUS

The primary purpose of the shock tube facility studied in this paper is investigation of the structural response of a circular plate resting on soil when subjected to a shock wave [25]. Investigation of the underground tunnel lining under blast and fire conditions represents the general framework in which the present shock tube was conceived. The innovative features of the shock tube are a suitable end-chamber designed to investigate soil-structure interaction and burner equipment to heat concrete specimens in order to study to what extent thermal damage can affect the transmitted and reflected pressure wave as well as the structural response.

A detailed description of the shock tube facility with emphasis placed on the principles that have driven the experimental design choices may be found in [25]; only the features of interest are summarized in the following description.

A schematic layout of the shock tube device in the assembled configuration ready to test a specimen is shown in Figure 1a. Four chambers, movable on a linear guide system, are shown in Figure 1a: (a) the driver section, (b) the buffer or diaphragm section, (c) the driven section, and (d) the specimen/soil section. The total length of the shock tube is 14.9 m.

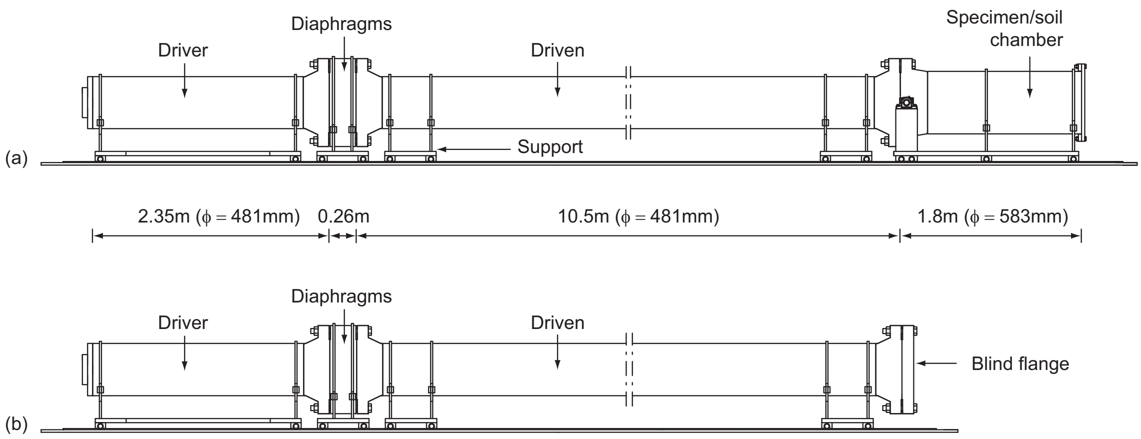

Fig. 1 Lateral view of the shock tube facility: (a) configuration with specimen/soil chamber and (b) configuration with blind end flange

The buffer chamber is located between the driver and driven chambers and two diaphragms are placed in it. The three chambers have a circular cross-section with an internal diameter of 481 mm. The gas used in the experiments is helium for the driver and buffer chambers, while the driven gas is air under ambient conditions.

The driver and driven chambers have a length of 2.35 m and 10.5 m, respectively, with a 13.5 mm thick wall, while the buffer chamber has a length of 260 mm. The external diameter of the buffer chamber is 857 mm, equal to the maximum diameter of the flange welded on the driver and driven extremities. The buffer chamber is separated from the driver and driven chambers by two scored steel diaphragms; a gasket is placed on each side of the diaphragms to guarantee seal during the experiments. When the twenty screws are tightened with an impact torque wrench, each edge of the buffer, driver and driven sections bites into the diaphragms, guaranteeing an effective seal between the different shock tube chambers.

One innovative feature of the shock tube is the specimen/soil chamber, which is 1.8 m long and 13.5 mm thick and has an inner diameter of 583 mm. The specimen/soil section can be connected to the driven section through an ad hoc flange welded at one of its extremities; a blind flange closes the other end of the chamber. The chamber contains a circular slab specimen continuously supported on the soil. Further details of the specimen/soil chamber may be found in [25].

In the present paper, the performance of the shock tube is not evaluated in the full configuration normally adopted during structural tests (Fig. 1a), but instead the specimen/soil chamber is substituted with a blind end flange (Fig. 1b). In this case, the blind end flange is connected to the end flange of the driven chamber and reproduces the ideal situation of a rigid end. In this way the source of dissipation given by the finite specimen/soil axial stiffness on the performance of the shock tube equipment does not need to be modeled.

2.1 Firing mechanism

Either a single or a double diaphragm mode can be adopted for each test run. In double diaphragm mode, which is the test procedure adopted in this study, the buffer chamber is filled with a gas at a pressure approximately equal to the average of the driver (p_4) and driven (p_1) gas pressure. When the gases reach the assigned pressure levels in both chambers, the gas in the buffer chamber is vented, allowing it to return to atmospheric pressure. At that instant, the differential pressure between the driver and the buffer sections exceeds the rupture pressure of the corresponding diaphragm, and the first diaphragm opens. As a consequence, when the pressure wave arrives at the second diaphragm's interface, the second diaphragm fails and the firing mechanism is completely activated.

As mentioned above, no breaking devices are used to force the diaphragms open. Diaphragms are in fact designed to break under a given pressure difference. All diaphragms used in this study are made of S235 JR structural steel in accordance with [49]. This choice of material was motivated by the fact that steel can guarantee a burst pressure in the range of interest with a small thickness. In addition, S235 JR steel is easily available and inexpensive. The diaphragms are of a circular shape with a diameter of 697 mm, and are obtained by laser cutting from hot rolled plates. On one surface of the diaphragm, two grooves are scored through a milling machine. The two grooves are inclined at 90° with respect to each other and cross the center of the diaphragm.

In this study, two different types of diaphragms with a thickness of 2 mm are used; they differ in score depth, which was equal to 1.3 and 0.8 mm, respectively. The two diaphragm types correspond to increasing levels of burst pressure and were used for the two different pressure combinations inside the driver and buffer chambers, as described in the following section.

2.2 Instrumentation and test program

In order to study shock tube performance, an appropriate set of instruments is applied to the tube. A set of three ICP (Integrated Circuit Piezoelectric) dynamic pressure transducers is positioned along the tube axis as indicated in Figure 2. The transducers (PT1-PT3) have a quartz sensing element with a full scale pressure of 6.9 MPa, a sensitivity of 0.7 mV/kPa, a rise time lower than 1 μs and a resonant frequency higher than 500 kHz.

Pressure transducer signal conditioning is performed by an ICP signal conditioner with gain equal to one, a bandwidth equal to 10 kHz and a broadband electrical noise equal to 3.5 μV rms.

All channels are acquired by means of the same data acquisition system with 56 parallel channels with a maximum sampling rate of 3 MS/s per channel and a 14-bit resolution. The data acquisition for all the channels is triggered by the signal of the first pressure transducer along the tube (PT1 in Fig. 2): when the measured pressure exceeds a threshold value indicating the arrival of the shock wave, the system starts acquiring data.

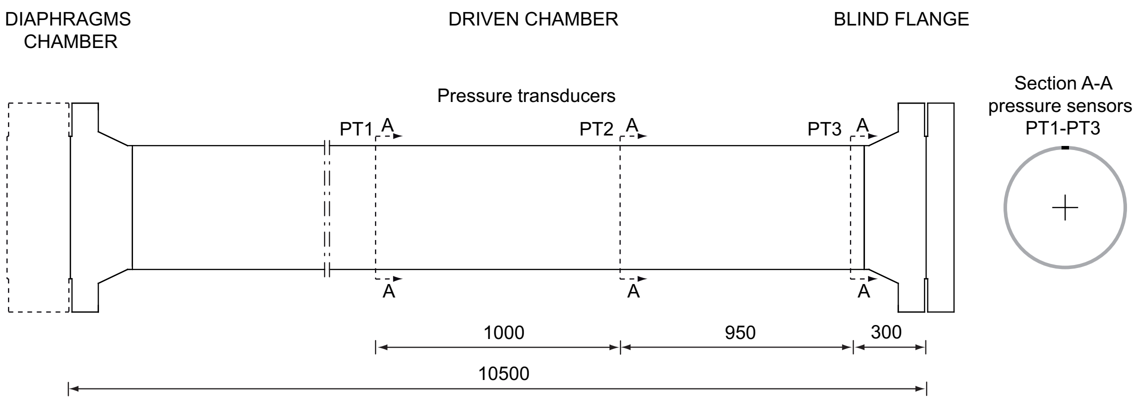

Fig. 2 Location of the instruments on the shock tube facility (units mm)

Two sets of experiments are discussed in this work, with different pressure levels inside the driver and buffer chambers. The first set of experiments, referred to below as low pressure experiments, adopt an absolute pressure of 5.4 and 3.2 bar inside the driver and buffer chambers, respectively. The second set of experiments, referred to as high-pressure experiments, adopt an absolute pressure of 15 bar inside the driver chamber and 8 bar inside the buffer chamber. In all the experiments the driven chamber contained air under ambient conditions, while the driver and buffer chambers were pressurized with helium after being vacuumed at about -800 mbar with respect to ambient pressure. A summary of the initial conditions inside the shock tube chambers during the two sets of experiments is reported in Table 1.

Experiment type	Driver		Buffer		Driven	
	pressure* (bar)	gas	pressure* (bar)	gas	pressure* (bar)	gas
Low pressure	5.4	helium	3.2	helium	1.01	air
High pressure	15	helium	8	helium	1.01	air

Table 1 Initial conditions inside the shock tube chambers during the two sets of experiments (* absolute pressure values)

3 FINITE VOLUME ONE-DIMENSIONAL SHOCK TUBE SOLVER

A finite volume approach (FV – 1D) is used to solve the one-dimensional inviscid flow within the shock tube and to compute the reference solution with zero losses.

The fluid is described as an ideal mixture of constant-specific-heat ideal gases, namely, air and helium. The mixture properties are computed as

$$p(T,\rho) = RT\rho \tag{1}$$

$$e(T) = c_v T \qquad c_v = \text{const} = \frac{R}{\gamma - 1} \tag{2}$$

$$p(e,\rho) = (\gamma - 1)\rho e \tag{3}$$

where p is pressure, ρ is density, T temperature, e internal energy per unit mass, c_v is specific heat at constant volume, c_p is specific heat at constant pressure and $\gamma = c_p / c_v$ is the specific heat ratio. Both R and γ are obtained by weighting pure-component values using mass-fraction.

To simplify the numerical scheme, diaphragm opening is assumed to be instantaneous and the buffer chamber is not explicitly included in the initial conditions. Therefore, a discontinuous initial condition is imposed at time t = 0, with the initial discontinuity located at the beginning of the driven section: p, T ρ and γ of both driver and driven gases are imposed at t = 0. Wall boundary conditions are imposed on both shock-tube ends.

A finite-volume Lax-Wendroff method is used to solve the one-dimensional unsteady Euler equations. Upwind stabilization is obtained by means of a Total Variation Diminishing (TVD) approach, where the high-order Lax-Wendroff flux is blended with the first-order Roe upwind scheme in the proximity of flow discontinuities. The switch is controlled by the van Leer limiter. Details of this standard Godunov scheme may be found, for instance, in [50].

A uniform grid of 1000 cells is used in all computations, with a Courant-Friedrichs-Lewy (CFL) number of 0.5. The corresponding time step is about 0.6×10^{-6} s in all simulations. The numerical solution over 1000 cells is almost undistinguishable from that obtained on the coarser and finer grids made of 500 and 2000 cells, respectively, thus confirming the grid independence of the reference solution.

4 NUMERICAL FE MODELS

Finite element numerical models are devised to reproduce wave pressure propagation inside the tube, the opening process of the diaphragm and fluid-structure interaction. The impulsive phenomena involved, and the need to reproduce fluid-structure interaction, led to the choice of the Finite Element explicit solver LS-DYNA [51].

All numerical analyses are carried out adopting a Lagrangian description for the shock tube structure and the steel diaphragms and a Eulerian domain for the gases contained in the shock tube chambers and the air outside the tube walls. An Arbitrary Lagrangian Eulerian (ALE) formulation is selected to describe the phenomenon of fluid-structure interaction. This choice allows the energy flux from gases to the structure after the opening of the diaphragms to be reproduced, permitting estimation of gas pressure loss and the stress field in the structure due to gas propagation along the tube.

4.1 Description of the models

The maximum test pressures obtainable in the facility and its global efficiency are evaluated using FE numerical models in which different sources of dissipation are included separately. The main characteristics of all the models are summarized in Table 2 and discussed below.

Mesh		Models				
		FE - 1D	FE - $3D_A$	FE - $3D_B$	FE - $3D_C$	FE - $3D_D$
Fluid	Element type	8-node hexahedron	8-node hexahedron	8-node hexahedron	8-node hexahedron	8-node hexahedron
	Element N.	2412	76608	76608	76608	52208
	Smallest size	2 x 2 x 0.5 cm	2 x 2 x 1.4 cm	2 x 2 x 1.4 cm	2 x 2 x 1.4 cm	2 x 2 x 1.4 cm
Shock-tube structure	Element type	Not included	Not included	3-node shells	3-node shells	Not included
	Element N.			46116	46116	
	Smallest size			1.3 cm	1.3 cm	
Diaphragms	Element type	Not included	Not included	Not included	Not included	4-node shells
	Element N.					5700
	Smallest size					1 x 1 cm

Table 2 Characteristics of the FE models adopted for numerical analyses

The first step in the numerical investigation consists in development of a one-dimensional model (in the following model FE – 1D) considering infinite stiffness of tube wall and instantaneous diaphragm opening without energy loss. The entire length of the three chambers is modeled using solid hexahedral elements, aligned in the axial direction. The only degree of freedom associated with the nodes is axial translation. Axial constraint is given to the eight nodes located at the extremities of the tube length. These constraint conditions lead to a pure 1D simulation, even though based on 3D elements. This choice is due to the best effectiveness of the 3D element formulation in this kind of problem. This approach permits reproduction of wave propagation affected only by chamber length, the nature of the gases and the initial conditions. The aim of this model is to evaluate the influence of the numerical approach adopted by comparing this solution to the one obtained with the finite volume presented in the previous section. A mesh sensitivity study is carried out using element sizes of 1 mm, 5 mm and 20 mm. The solution is found to be almost independent of mesh size.

In order to verify the quality of the 3D mesh in reproducing the gas volume contained in the real device geometry, a gas-only 3D model (referred to as model FE – $3D_A$ below) is created. A second 3D model, referred to as model FE – $3D_B$, is devised including the tube wall and the Fluid-Structure Interaction (FSI). With the aim of verifying the FSI algorithm adopted, model FE – $3D_B$ considers the limiting situation of an infinitely stiff tube wall that represents the same condition as model FE – $3D_A$ and should therefore produce the same results. Infinite stiffness of the tube wall is achieved by the introduction of additional constraints that fix all the nodes of the tube wall to the ground.

The additional constraints included in model FE – $3D_B$ are removed in a third model (referred to as Model FE – $3D_C$) simulating finite stiffness of the shock tube structure. The pressure disturbances propagating within the shock tube cause the tube walls to vibrate, so that a part of the gas's internal energy is dissipated by means of elastic tube strain energy.

In the aforementioned models (FE – $3D_A$, FE – $3D_B$ and FE – $3D_C$), the gases are modeled using solid hexahedral elements filling the internal chambers and a small layer of air outside the tube; external air layer is only included in models FE – $3D_B$ and FE – $3D_C$. This external layer is necessary to allow wall displacement, since, in the FSI approach adopted here, the Lagrangian mesh describing the structure moves within the Eulerian mesh describing the fluid. The shock tube structure (models FE – $3D_B$ and FE – $3D_C$) is modeled using solid elements and shell elements with 3 integration points through the thickness. The mechanical interaction between the gases and the structure is obtained using the ALE approach. In model FE – $3D_C$ the shock tube structure can move along its axis, as in the experiments (see Section 2). An external view of the finite element model FE – $3D_C$ is given in Figure 3a, while Figure 3b provides a vertical cross section of the model in which gases under different conditions are denoted with different colors.

The reduction of performance due to the diaphragm opening mechanism is analyzed by modeling the firing mechanism. To this aim a further 3D model is created (in the following model FE – $3D_D$), in which the gases are modeled using solid hexahedral elements filling the internal chambers. The two steel diaphragms are represented using shell elements, while the shock tube structure is not taken into consideration, and is replaced by boundary conditions imposed on the gas domain. Also in this model, mechanical interaction between gases and diaphragms is achieved by means of the ALE approach. To reduce the computational burden, the opening mechanism of the diaphragms is modeled by almost instantaneous venting of the buffer chamber (about 1 ms). The firing mechanism is implemented in the FE – $3D_D$ analysis by a sudden reduction of the internal energy in the intermediate chamber gas, so that in 1 ms the value of the intermediate chamber pressure drops to the atmospheric value. By design, the buffer venting results in a larger pressure difference across the diaphragms; a failure criterion associated with the material allows the diaphragm to petal by means of activation of element erosion when the maximum allowed plastic strain on the material is reached without any damage evolution law.

In all the models, the simulation starts with the three chambers at the design pressures: namely, the driver chamber at the maximum pressure, the intermediate chamber at the intermediate pressure and the driven chamber at atmospheric pressure.

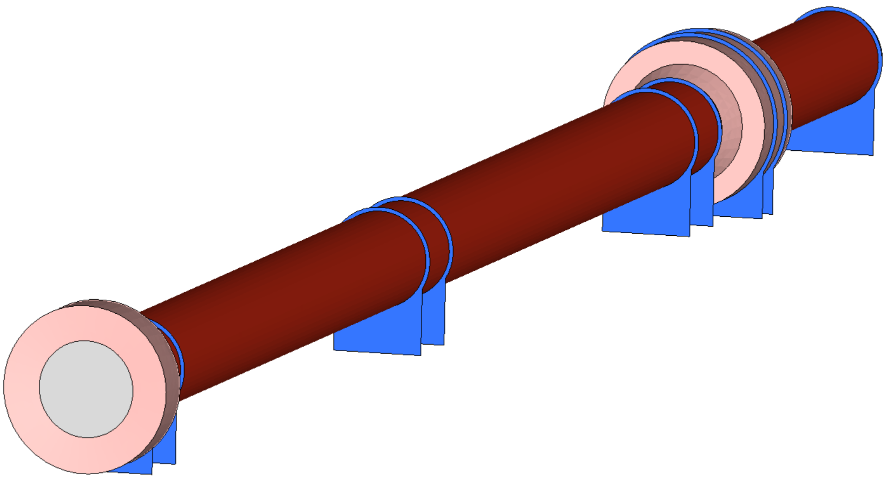

(a)

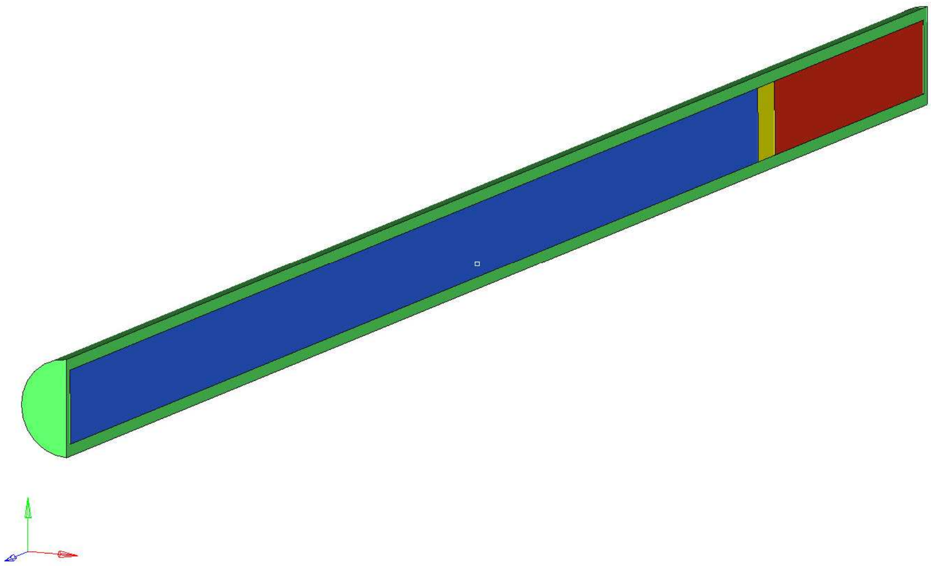

(b)

Fig. 3 Finite element model: (a) external view of the Lagrangian domain including the whole structure; (b) vertical section of the Eulerian domain including all the gases: red, yellow and blue represent respectively the gases inside driver, buffer and driven chamber, while green volume represents the air outside the shock-tube

4.2 Materials and equation of state

This section describes the constitutive laws and the equation of state for each material (fluid: air and helium; shock tube structure; steel diaphragms).

4.2.1 Fluid

For the gases (air and helium) contained in the shock tube chambers and for the external air surrounding the shock tube, a *MAT_NULL material, considered as inviscid, is adopted. A linear polynomial Equation of State for linear internal energy, given by the following expression, is introduced:

$$p = C_0 + C_1 m + C_2 m^2 + C_3 m^3 + \left(C_4 + C_5 m + C_6 m^2\right) e \tag{4}$$

where $m = \rho / \rho_0 - 1$ being ρ / ρ_0 the ratio of the current to the initial density and $C_i \left(i = 0 - 6\right)$ are the polynomial coefficients. A model for a constant-specific-heat ideal gas is obtained by setting the coefficients in (4) equal to $C_0 = C_1 = C_2 = C_3 = C_6 = 0$ and $C_4 = C_5 = \gamma - 1$.

Each chamber is initialized by imposing the density, specific heat ratio, specific internal energy, and initial pressure values reported in Table 3. The temperature inside and outside the shock tube chambers is initially assumed to be equal to 293.15 K.

4.2.2 Steel shock tube components

Having designed the shock tube facility to operate in the elastic regime over the full range of service pressures, a linear elastic material (*MAT_ELASTIC) is assumed for all shock-tube components and the corresponding material properties are listed in Table 4.

Experiment type			Driver gas (Helium)	Buffer gas (Helium)	Driven gas (Air)
Low pressure	Specific heat ratio γ	(-)	1.668	1.668	1.4
	Density ρ_0	(kg/m^3)	0.889	0.528	1.204
	Pressure p	(MPa)	0.541325	0.321325	0.101325
	Specific internal energy E_0	(kJ/m^3)	810.64	481.19	253.36
High pressure	Specific heat ratio γ	(-)	1.668	1.668	1.4
	Density ρ_0	(kg/m^3)	2.465	1.316	1.204
	Pressure p	(MPa)	1.501325	0.801325	0.101325
	Specific internal energy E_0	(kJ/m^3)	2248.25	1199.993	253.36

Table 3 Fluid initialization properties

		Steel shock tube structure	Steel diaphragms
Material type	(-)	*MAT_ELASTIC	*MAT_PLASTIC_KINEMATIC
Density ρ	(kg/m^3)	7850	7850
Young modulus E	(MPa)	210000	210000
Poisson ratio ν	(-)	0.33	0.33
Yield stress	(MPa)	-	355
Tangent modulus E_t	(MPa)	-	806
Ultimate strain	(%)	-	24.8

Table 4 Material parameters adopted for the shock tube structure and diaphragms

4.2.3 Steel diaphragms

Two scored steel diaphragms made of S235 JR steel are modeled with a simple elastic-plastic material (*MAT_PLASTIC_KINEMATIC) characterized by linear kinematic hardening associated with the erosion of elements upon reaching failure strain. In Table 4, E_t indicates the slope of the bilinear stress strain curve. For both types of diaphragm, referred to below as type A and B for diaphragms used in low and high pressure experiments, respectively, a small specimen having the same thickness as the diaphragms is extracted from the same plate as was used to obtain the diaphragms. The specimens, 300 mm long and 20 mm wide, are tested under uniaxial tension following the standard tensile tests described in UNI EN ISO 6892-1 [52]. The nominal stress – strain curves obtained from the tensile tests on the two small specimens are converted into true stress – true strain curves (Fig. 4) according to the following relationships:

$$\varepsilon = \ln\left(1+\varepsilon_{nom}\right) \tag{4}$$

$$\sigma = \sigma_{nom}\left(1+\varepsilon_{nom}\right) \tag{5}$$

where ε_{nom} and σ_{nom} represent nominal strain and stress. The yield stress and the ultimate strain adopted in the analyses are derived from Figure 4. All material properties used for the diaphragms are reported in Table 4.

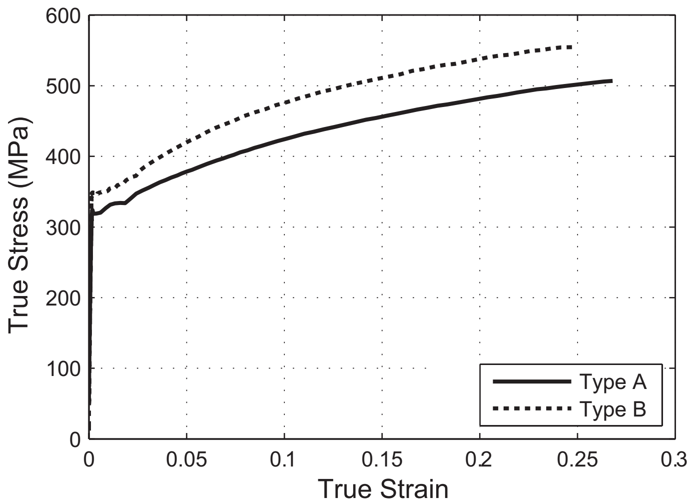

Fig. 4 Uniaxial tensile true stress-true strain curves used for diaphragm types A and B

5 RESULTS AND DISCUSSION

In this section, the results of the FE numerical models are first compared to the reference finite volume solution presented in Section 3 (model FV – 1D). The most representative model results (model FE – $3D_D$) are then compared with the experimental data.

The experimental measurements together with the results of all the numerical models are summarized in Tables 5 and 6, for low and high pressure conditions respectively. In these tables, p_i and p_r refer to the incident and reflected pressures, respectively, and the subscript j ($p_{j=1-3}$) refers to the position along the driven chamber, with reference to the position of transducers PT1-PT3 (see Fig. 2). In addition, Tables 5 and 6 report the incident (v_i) and reflected (v_r) wave velocities calculated as the average along the driven chamber in the space between transducers PT1 and PT2 (v_{i1} and v_{r1}) and between transducers PT2 and PT3 (v_{i2} and v_{r2}).

	p_{i1} (MPa)	p_{i2} (MPa)	p_{i3} (MPa)	p_{r1} (MPa)	p_{r2} (MPa)	p_{r3} (MPa)	v_{i1} (m/s)	v_{i2} (m/s)	v_{r1} (m/s)	v_{r2} (m/s)
FV - 1D	0.21	0.21	0.21	0.26	0.37	0.59	570.15	576.59	463.82	397.22
FE - 1D	0.22	0.22	0.20	0.25	0.35	0.55	571.49	574.92	449.42	391.69
FE - $3D_A$	0.22	0.21	0.20	0.25	0.35	0.54	563.48	576.46	438.60	401.01
FE - $3D_B$	0.22	0.21	0.20	0.24	0.34	0.54	555.74	576.81	432.34	391.27
FE - $3D_C$	0.22	0.21	0.20	0.24	0.34	0.54	555.52	576.81	432.34	391.43
FE - $3D_D$	0.12	0.11	0.11	0.18	0.23	0.28	450.31	494.82	347.21	363.91
Experimental	0.13	0.13	0.13	0.19	0.25	0.28	501.00	453.03	380.37	364.26

Table 5 Incident and reflected peak pressure (p_i, p_r) and wave velocity values (v_i, v_r) under low pressure conditions (FV = Finite Volume; FE = Finite Element)

	p_{i1} (MPa)	p_{i2} (MPa)	p_{i3} (MPa)	p_{r1} (MPa)	p_{r2} (MPa)	p_{r3} (MPa)	v_{i1} (m/s)	v_{i2} (m/s)	v_{r1} (m/s)	v_{r2} (m/s)
FV - 1D	0.48	0.48	0.48	0.80	1.22	1.96	764.34	779.58	543.84	454.39
FE - 1D	0.48	0.52	0.48	0.74	1.13	1.83	768.58	776.27	540.66	446.64
FE - $3D_A$	0.49	0.49	0.49	0.72	1.12	1.82	759.59	789.04	520.02	459.38
FE - $3D_B$	0.49	0.49	0.48	0.67	1.03	1.73	740.69	791.01	498.01	439.61
FE - $3D_C$	0.48	0.48	0.48	0.65	1.01	1.71	740.87	791.01	498.01	433.79
FE - $3D_D$	0.32	0.31	0.30	0.50	0.76	0.99	606.02	673.81	416.74	395.83
Experimental	0.37	0.27	0.46	0.64	0.64	1.15	613.12	703.70	431.03	390.95

Table 6 Incident and reflected peak pressure (p_i, p_r) and wave velocity values (v_i, v_r) under high pressure conditions (FV = Finite Volume; FE = Finite Element)

Figure 5 shows a comparison of the pressure time history for pressure transducers PT1-PT3 between the reference FV – 1D model (dashed line) and the FE – 1D model (continuous line) under low and high pressure conditions (see Table 1). The pressure signals for the finite volume and the finite element 1D models are almost indistinguishable in both the low and high pressure conditions, thus confirming the applicability of the FE approach to study such phenomena. In the following, all pressure signals are synchronized in correspondence with the incident shock wave passage through transducer PT1.

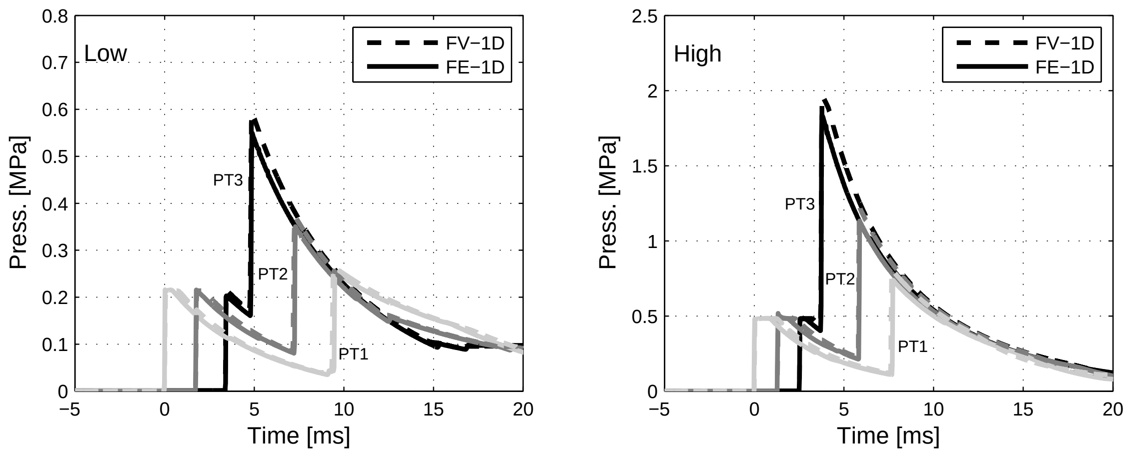

Fig. 5 Pressure time history comparison between FV – 1D (dashed line) and FE – 1D numerical model (continuous line) for pressure transducers PT1-PT3: (a) low and (b) high pressure experiments

In Figure 5, the pressure signal PT1 shows the passage of the incident shock wave, which is followed by a region of constant pressure. Then pressure decreases due to the arrival of the rarefaction wave, which is reflected at the end wall of the driver chamber. The pressure increases again as the shock wave reaches position PT1, after being reflected at the driven-section end-wall. The reflected shock is immediately followed by the reflected rarefaction wave, this time reflecting off the driven section end-wall. The interaction between the reflected shock and rarefaction is clearly visible in Figure 5. A similar profile is predicted at positions PT2 and PT3 in the high pressure scenario; in the low pressure scenario, the interaction between the shock and the rarefaction wave is already visible at stations PT2 and PT3.

In order to evaluate the accuracy of the models (models FE – $3D_A$ and FE – $3D_B$) and separately assess the influence of the different sources of non-ideality discussed in Section 4 (models FE – $3D_C$ and FE – $3D_D$), namely, tube vibration, finite wall stiffness and the diaphragm opening mechanism, the numerical results from the diverse models responses are compared to the FE – 1D model.

Figure 6 compares the pressure time history of the numerical models FE – 1D and FE – $3D_A$ at 300 mm upstream of the driven end-wall (PT3 location) under low and high pressure conditions. The response of the two models is almost indistinguishable in both cases with a maximum difference of the peak reflected pressure between the two models equal to about 1.5%, thus assessing the correctness of use of a three-dimensional description in model FE – $3D_A$.

The correctness of the FSI algorithm, disregarding finite tube wall stiffness, is assessed in Figure 7 by comparing the pressure time history of the numerical models FE – 1D and FE – $3D_B$ at location PT3 under low and high pressure conditions. Under low pressure, introduction of the FSI has practically no effect with respect to the previous model, as is apparent in Figure 6a and Figure 7a. Under high pressure, the FSI has a minor effect on the model’s response, shifting the difference in terms of peak reflected pressure from approximately 1% to 5%, respectively between models FE – 1D and FE – $3D_A$ (Fig. 6b) and between FE – 1D and FE – $3D_B$ (Fig. 7b). These results prove the correctness of the FSI algorithm for the limiting condition of an infinitely stiff tube wall.

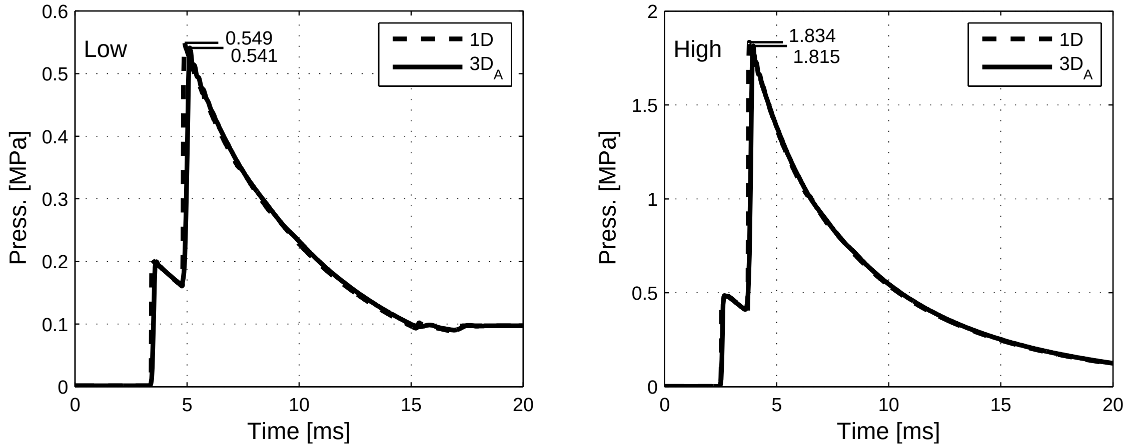

Fig. 6 Pressure time history comparison between numerical FE models 1D and $3D_A$ for pressure transducer PT3: (a) low and (b) high pressure experiments

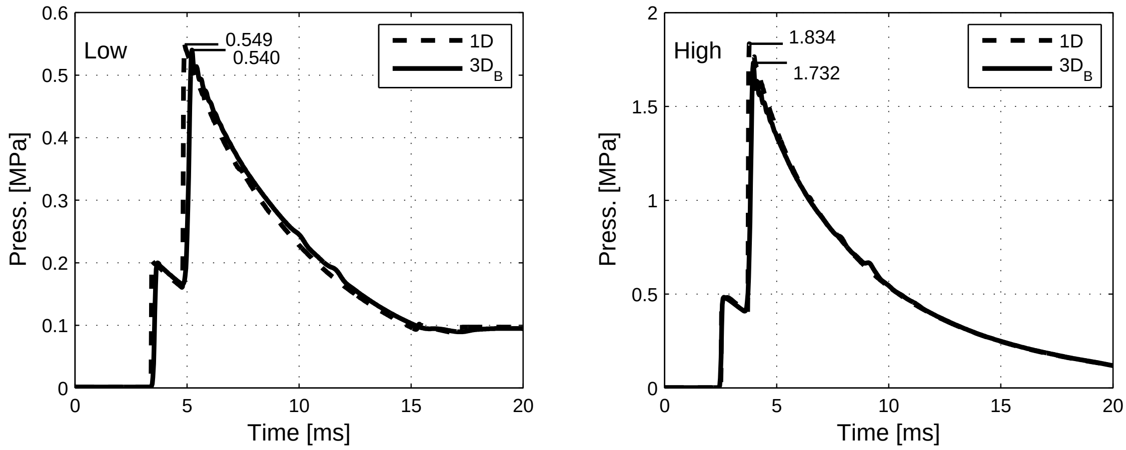

Fig. 7 Pressure time history comparison between numerical FE models 1D and $3D_B$ for pressure transducer PT3: (a) low and (b) high pressure experiments

Figure 8 compares the pressure time history of the numerical models FE – 1D and FE – $3D_C$ at location PT3 under low and high pressure conditions. In model FE – $3D_C$, finite tube stiffness is found not to significantly affect the peak value of reflected pressure. In particular, under low pressure conditions, model FE – $3D_C$, as previous 3D models, computes a peak value of the reflected pressure that is 1.5% lower with respect to the FE – 1D model; under high pressure this difference is about 7%. The results of FE – $3D_B$ and FE – $3D_C$ models are almost identical and are characterized by the same difference with respect to the FE – 1D model. This difference is mainly due to the introduction of the FSI effect (difference of about 5% between models FE – 1D and FE – $3D_B$) rather than finite tube stiffness (difference equal to approximately 1% between FE – $3D_B$ and FE – $3D_C$ peak reflected pressure). However, it is worth noting that the differences seen between the FE – $3D_A$, FE – $3D_B$ and FE – $3D_C$ models are in the order of the numerical uncertainly in the simulations (grid resolution, etc.).

Figure 8 shows that for the pressure values under study and the shock tube's geometric characteristics, finite tube stiffness has a negligible effect because of low deformation. This result is also confirmed by a simple analytical derivation detailed in Appendix A, where it may be observed that the maximum cross section area percentage variation of the tube is less than 0.066% in all the cases considered. Comparison of the maximum radial displacement obtained with the numerical FE – $3D_C$ model and the analytical one reported in Appendix A respectively confirms the validity of the FE model.

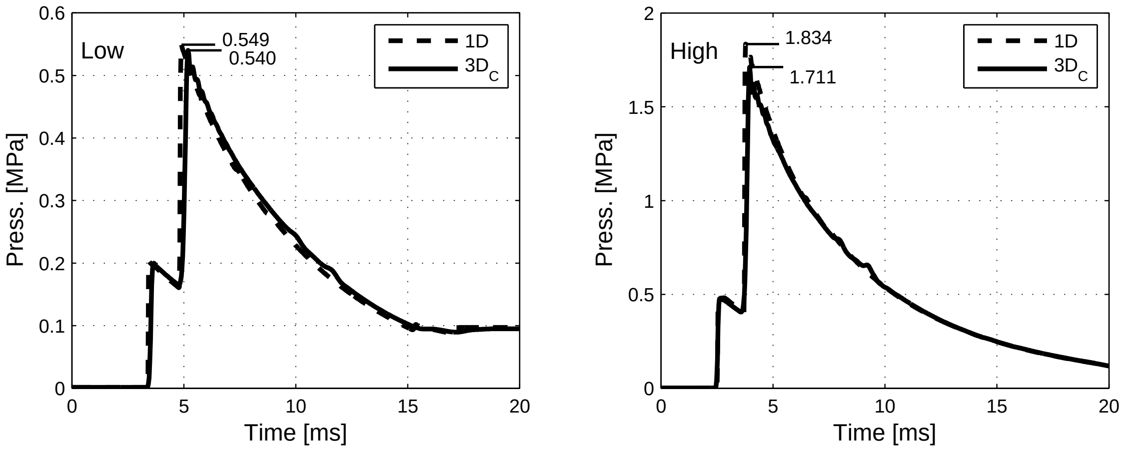

Fig. 8 Pressure time history comparison between numerical FE models 1D and $3D_C$ for pressure transducer PT3: (a) low and (b) high pressure experiments

Figure 9 shows the pressure signal history for models FE – 1D and FE – $3D_D$ at the same PT3 location. The diaphragm opening mechanism strongly influences the pressure signal history. The opening mechanism of the diaphragm leads to a reduction of both incident and reflected peak pressure with respect to the reference values. In the low pressure scenario, the incident and reflected pressure reductions are about 50% with respect to the reference values, whereas in the high pressure scenario the incident and the reflected peak pressure differences are equal to 38% and 46% of the corresponding reference case values, respectively.

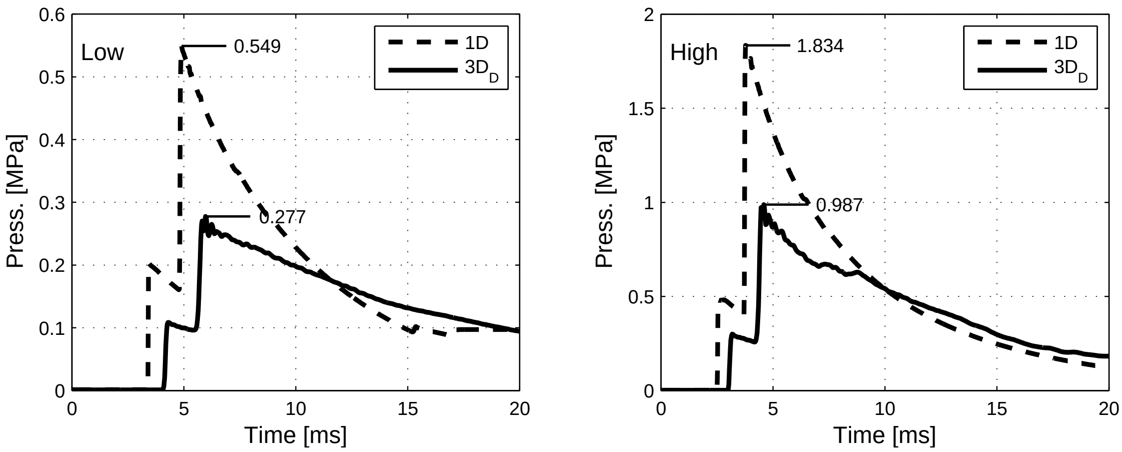

Fig. 9 Pressure time history comparison between numerical FE models 1D and $3D_D$ for pressure transducer PT3: (a) low and (b) high pressure experiments

For complete petalling, the open area is equal to that of the square inscribed in the circular cross-section, namely, the ratio of the open area to the cross-sectional area is $2/\pi$ or 64%. In the actual experiment, this ratio is found to be close to 50%. A rough estimate of pressure peak reduction due to the incomplete petalling may be obtained from the empirical relation presented in [46], which provides a 5% reduction for complete petalling (64% open area) and a 10% reduction for a 50% opening.

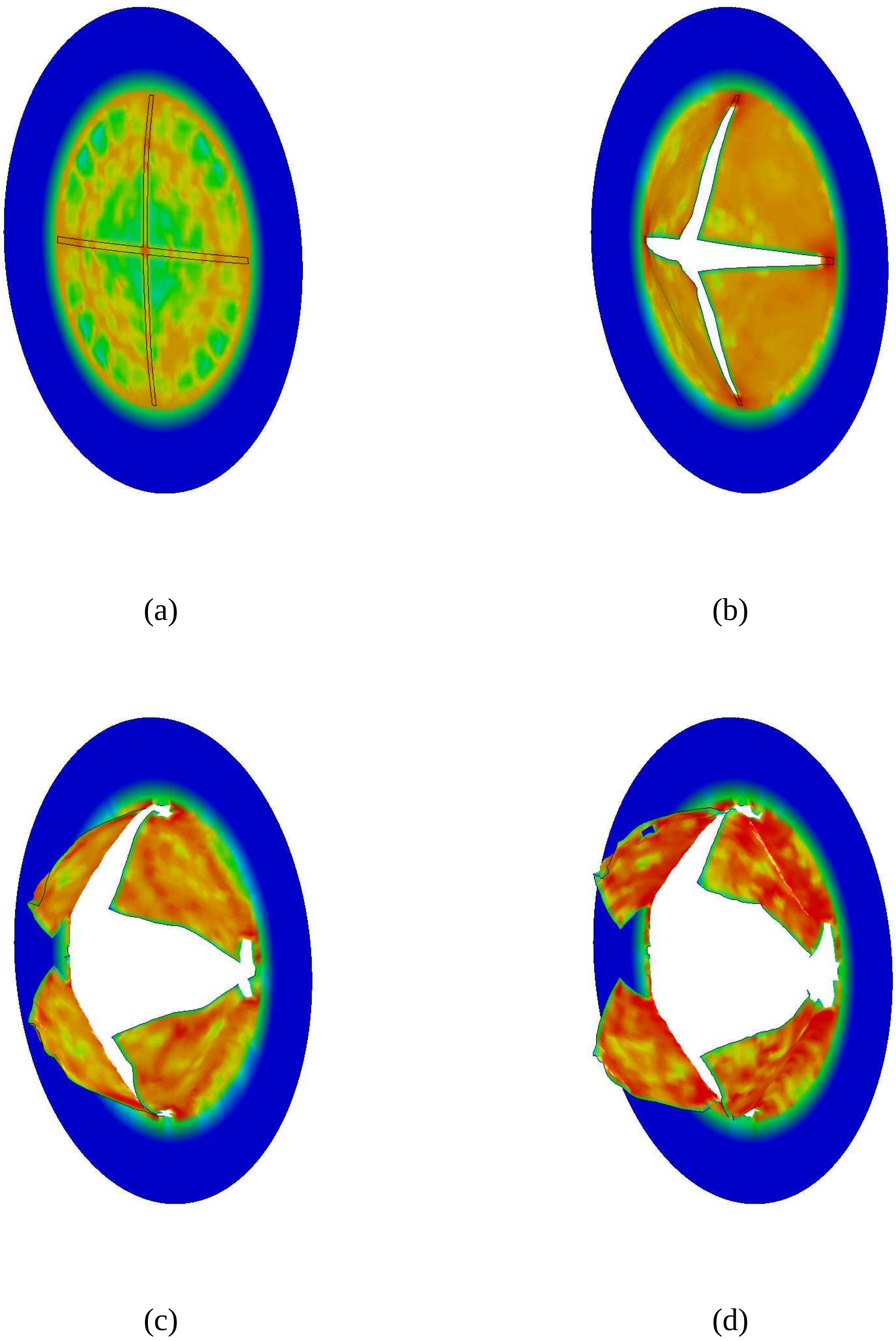

Fig. 10 Diaphragm opening mechanism during FE analyses: (a) plate to membrane transition behavior at 1.2 ms, (b) tearing propagation (2.4 ms) and (c-d) petal formation (3.6 ms and 7.2 ms). Contour represents the Von Mises stress field, with red associated with the maximum value. In a), b) and c) maximum Von Mises is 555 MPa. In frame d) maximum Von Mises value is 498 MPa

The FE analysis illustrates diaphragm transition from plate to membrane behavior, characterized by the formation of negative plastic hinges along the diaphragm's clamped edge followed by yielding of the whole petal region, resulting in formation of the deformed shape typical of the membrane regime (Fig. 10a). Numerical results reveal that tearing occurs propagating from the central region of the diaphragm at the intersection of the grooves toward the fixed edges (Fig. 10b). The opening process concludes with complete petal formation (Fig. 10c-d).

The significant differences between the ideal pressure and the estimated pressures pose a serious question about which specific phenomena lead to the observed non-ideal pressure losses.

Available literature explains the non-ideality of the real shock-tube pressure measurements by also including fluid-dynamic disturbance due to the partial opening of the diaphragm, which results in a sudden diameter restriction interrupting the regular section of the tube and which is characterized by the percentage of section reduction measured at the end of each test [41-46].

Gaetani et al. [46] show an empirical correlation between the percentage of section reduction at the end of the tests and the pressure loss measured, permitting estimation of shock tube performance with no need to investigate the opening mechanism in detail.

The approach in [46] is developed from experimental and simulation data obtained in a tube 80 mm in diameter loaded with air at a pressure of around 100 kPa and thin polymeric diaphragms characterized by an average opening time around 0.3 ms with a constant flow duration of about 7 ms. Under these operating conditions, the disturbance caused by the dynamics of the opening mechanism is very limited due to the short opening time (about 7 ms), because most of the mass has passed through the diaphragm section when the opening mechanism is terminated.

On the contrary, the case considered in this paper is characterized by an ideal pressure profile with a “triangular” shape, an overall duration of about 5-7 ms and a firing mechanism that takes more than 3-4 ms to be completed, with the first phase characterized by an orifice behavior which gradually releases pressure, guiding the flux to a resulting “cone shaped” flux front. This relatively long partial release of pressure, with almost the same duration as the ideal flux, indicates that in the present case, the dynamics of the opening process cannot be disregarded without overestimating the pressure peak.

This will be evident if we compare the ideal pressure curves with the experimental ones. The effect of the slow release of pressure causes the pressure to reduce during the first 5-7 ms, corresponding to a time span consistent with the expected duration of the actual diaphragm opening process, and then to increase slightly over time, because of the slow flux release.

Considering the FE – $3D_D$ simulations and focusing on the evolution of the pressure field during the diaphragm opening process, it will be apparent that the first compression wave starts propagating in the driven chamber when the opening process is still in its early stages. In fact, looking at the timing of the opening process in Figure 10, the first significant venting section is created at 2.4 ms, but, due to the significant inertia of the steel diaphragms and the ductile fracture mechanism, the complete opening process happens almost 5 ms later. This period of time during which a vent is opened but the opening process is not complete allows pressure to start propagating slowly, thus introducing non-ideality.

In particular, the results of the FE – $3D_D$ simulations clearly show that, right after the beginning of the fracture, the flow through the small (growing) orifice generates the first semi-spherical waves to propagate in the driven chamber. This first phase causes non-ideal (non-planar) wave fronts in both the compression and rarefaction waves, which will stabilize during propagation on a planar wave characterized by low pressure and speed, similar to that observed in the dynamic simulations in [44].

Depending on the diaphragm material, design and conditions, the orifice formation phase continues till the balance of pressure and fracture progress causes the diaphragm to petal and increase the venting flow. During this phase, the maximum flux of energy is released, forming additional pressure perturbations reflecting against the driven end-wall and reaching the maximum pressure rate. Maximum flux is released when the petals are still moving, thus indicating that the final deformation of the diaphragms is less relevant than the case considered in [46], and that in the present case, opening dynamics are driving tube non-ideality.

Pressure rates $\mathrm{d}p/\mathrm{d}t$ are thus directly related to $\mathrm{d}A(t)/\mathrm{d}t$, where $A(t)$ represents the function describing the section of the orifice generated by fracture propagation and bending of the petals.

Looking at the values reported in Tables 5 and 6, model FE – $3D_D$ best represents the experimental evidence. For this reason, comparison of the results of this model with the experimental pressure recorded by transducers PT1, PT2 and PT3 is shown in Figures 11-13, respectively. With the exception of transducer PT2 under high pressure conditions (Fig. 12b), where the model overestimates the experimental data, in all other cases the FE numerical model underestimates the experimental incident and reflected peak pressures. Under low pressure conditions, the numerical model provides a good prediction of the experimental response with a maximum relative difference in the incident peak of about 14% (Fig. 12a) and of 10% for the reflected peak pressure (Fig. 12a) for all pressure transducers. Under high pressure conditions the numerical model departs more significantly from the experimental data: a maximum relative difference of about 35% (Fig. 13b) and of 23% (Fig. 11b) is found for the incident and the reflected peak pressures, respectively. The good estimation of the incident and reflected peak pressures provided by the model FE – $3D_D$ with respect to the experimental measurements justifies good prediction of the incident and reflected wave velocities, where a time delay is barely detectable between the numerical and the experimental signals.

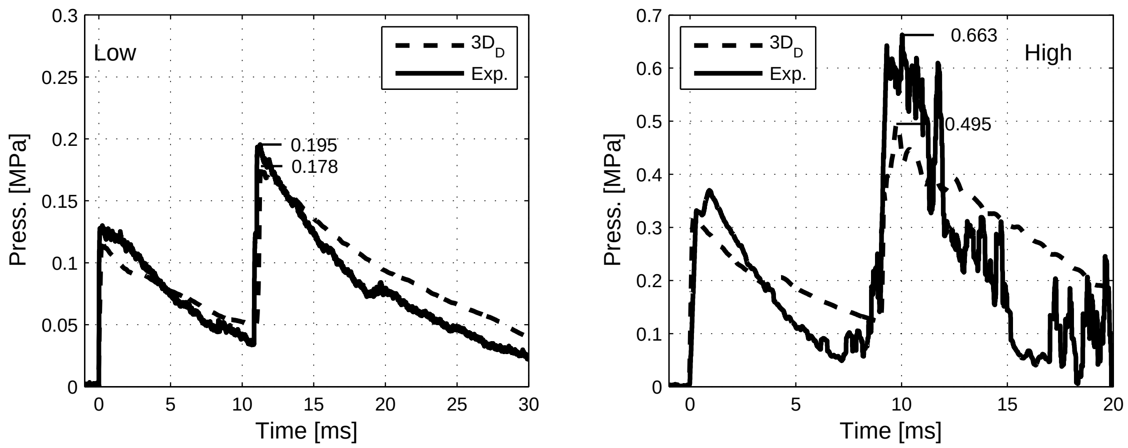

Fig. 11 Pressure time history comparison between experimental data and numerical model FE – $3D_D$ for pressure transducer PT1: (a) low and (b) high pressure experiments

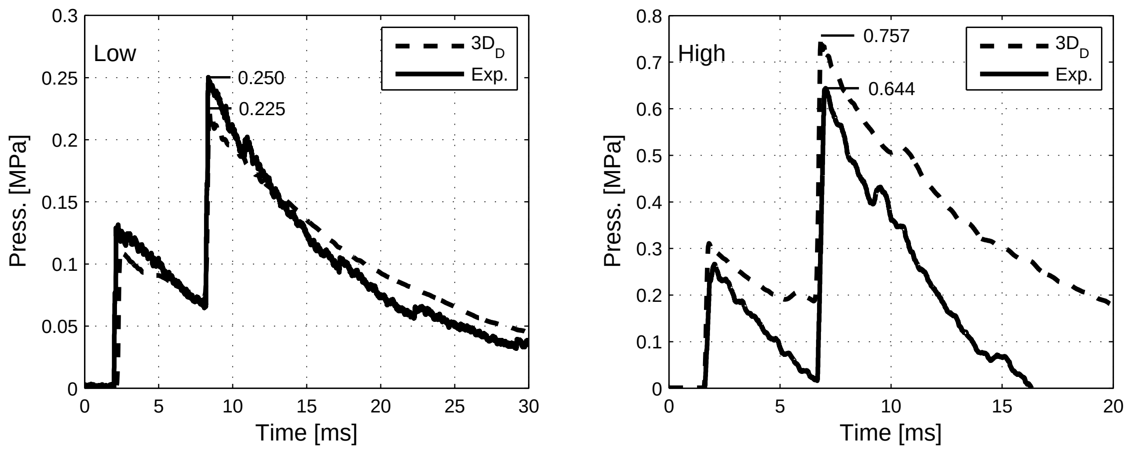

Fig. 12 Pressure time history comparison between experimental data and numerical model FE – $3D_D$ for pressure transducer PT2: (a) low and (b) high pressure experiments

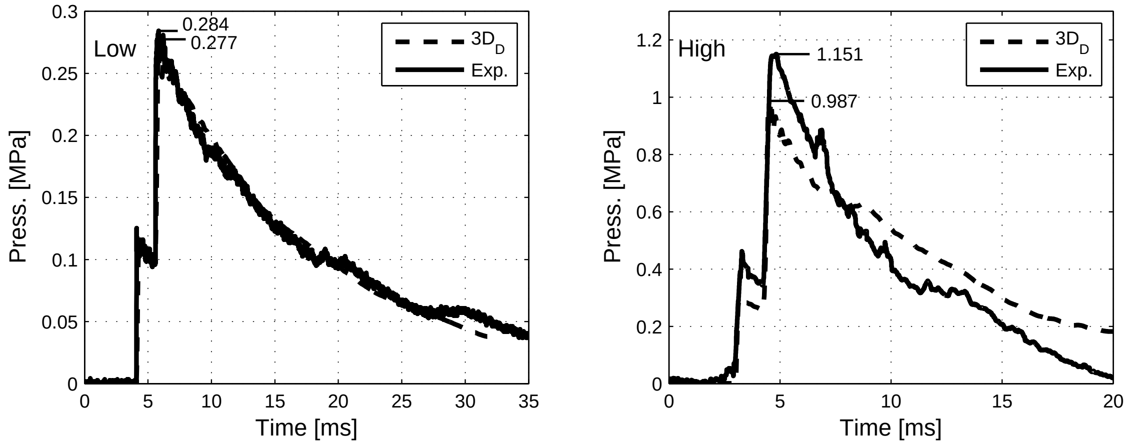

Fig. 13 Pressure time history comparison between experimental data and numerical model FE – $3D_D$ for pressure transducer PT3: (a) low and (b) high pressure experiments

A more quantitative yet concise shock tube performance indicator is the ratio between the value of peak pressure obtained from either experiments or numerical simulations and the corresponding reference pressure (Table 7).

	Low pressure test		High pressure test	
	η_{pi} (%)	η_{pr} (%)	η_{pi} (%)	η_{pr} (%)
FE – 1D	100.93	92.89	100.21	93.22
FE – $3D_A$	101.17	91.54	100.48	92.46
FE – $3D_B$	102.43	91.39	100.79	88.23
FE – $3D_C$	102.43	91.39	99.92	87.16
FE – $3D_D$	53.74	46.87	65.22	50.43
Experimental	59.53	48.10	76.56	58.63

Table 7 Numerical and experimental efficiency with respect to FV – 1D values for incident peak pressure (η_{pi}), reflected peak pressure (η_{pr}) and incident wave velocity (η_{vi})

This ratio is referred to as shock tube efficiency η and is evaluated for incident peak pressure ($\eta_{pi} = \left(p_i^j - p_i^{FV-1D}\right)/p_i^{FV-1D}$; j = FV-1D, FE-1D, FE-3DA, … , etc.) and reflected peak pressure ($\eta_{pr} = \left(p_r^j - p_r^{FV-1D}\right)/p_r^{FV-1D}$). In the experiments, reflected peak pressure efficiency is about 50% and 60% for low and high pressure conditions respectively. The reflected peak pressure efficiency evaluated for model FE – $3D_D$ is equal to 47% and 50% under low and high pressure conditions, respectively.

The larger efficiency observed in the experimental reflected pressure for the high pressure tests is possibly due to a faster diaphragm opening process. In fact, as already discussed in Section 2.1, the diaphragms used for low and high pressure tests are characterized by the same thickness but different score depth. This means that the masses of the diaphragms and the energy needed to create negative plastic hinges in the petalling formation are similar for both types of diaphragms (Fig. 10). This fact, combined with the different energies initially stored in the driver chamber, leads to lower opening times for high pressure tests and a consequent higher efficiency in terms of reflected pressure.

In comparison to most gas dynamic shock tubes, in the shock tube under study boundary layer losses do not represent a major factor due to the large diameter to length ratio, and can thus be neglected. The influence of boundary layer losses on incident peak pressure value is discussed in Appendix B.

6 CONCLUSIONS

The present work reports on the performance of a double diaphragm shock tube facility adopted for structural response investigations. For this purpose a performance indicator is introduced that accounts for pressure losses at the tube end-wall, where, unlike standard shock tubes, the material specimen is tested.

A numerical approach based on several finite element models of increasing complexity is proposed to expose the different sources of losses. The models accounts for several sources of dissipation, including tube wall vibration, finite tube stiffness, the boundary layer and the diaphragm opening mechanism. The models allowed us to estimate the different contributions to the overall efficiency of the device. Two parameters are considered in order to evaluate device efficiency: incident and reflected peak pressures.

Comparison of the reference one-dimensional finite volume results with the experimental ones revealed that the shock tube device under study has an efficiency in terms of reflected peak pressure ranging between 50% and 60% for low and high pressure tests respectively. The numerical results indicate that the most relevant source of dissipation is represented by the diaphragm opening process. Indeed, the numerical model including only the effects of diaphragm opening (model FE – $3D_D$), reproduces experimental pressure time history responses fairly well, with a maximum error in reflected peak pressures in proximity of the tube end-wall of about 14%.

ACKNOWLEDGMENTS

The research was financially supported by European INTERREG IT/CH 2006_2013 project ACCIDENT ID 7629770, Measure 2.2. The authors would like to thank an anonymous reviewer for providing the analysis of the tube deformation reported in Appendix A and for the insightful observations and helpful comments. The help of Luca Virtuani in implementing the Mirels' model simulations is also acknowledged.

APPENDIX A

An estimate of the tube expansion under static and dynamic conditions is reported in the following appendix.

The shock tube examined in this work can be considered a thin-walled cylinder where the hoop stress can also be assumed to be constant throughout the thickness. For this reason, the hoop stress (σ_h) in static conditions is given by the well-known equilibrium equation:

$$\sigma_h = \frac{p_{\text{int}} r_0}{h} \tag{A1}$$

where p_{int} represents the internal pressure, which is considered here, for the sake of simplicity, to be the peak reflected pressure; the internal pressures considered are those obtained from the FV – 1D model (see Tables 5 and 6), equal to 0.59 MPa and 1.96 MPa for the low and high pressure scenarios, respectively. In the same equation, r_0 represents the internal radius (r_0 = 240.5 mm) and h the tube wall thickness (h = 13.5 mm). The circumferential strain ε_h is equal to:

$$\varepsilon_h = \frac{\sigma_h}{E_s} \tag{A2}$$

where E_s is the steel's Young Modulus (E_s = 210000 MPa). Applying equations (A1) and (A2) to the high pressure scenario, the percentage of circumference variation is equal to 0.0166%, while the cross sectional area varies by $(1+\varepsilon_h)^2$, corresponding to a percentage area variation of 0.033%.

The static loading case may be generalized to a dynamic situation by considering the tube elastic and taking inertia into account. Applying Newton's second law in the radial direction and using the small angle approximation [33], it is possible to obtain the following Ordinary Differential Equation:

$$\ddot{r}(t) = \frac{p_{\mathrm{int}}\, r(t)}{r_0 h \rho_s} - \frac{E_s}{\rho_s}\left(\frac{1}{r_0} - \frac{1}{r(t)}\right) \tag{A3}$$

where *r(t)* is the time varying radius of the tube and ρ_s is the density of the tube material (ρ_s = 7850 kg/m^3). In this equation, a constant value of internal pressure over time is assumed, since a very short integration period is considered (0.5 ms). Integrating equation (A3), the maximum tube radius expansion reaches a value of twice the value estimated under static conditions (i.e., radius increases by about 0.08 mm in the high pressure scenario); the maximum increase in tube cross-sectional area is then equal to 0.066%.

The tube variation expansion histories under low and high pressure conditions are shown in Figure A1; in this figure, simple harmonic oscillator behavior under dynamic conditions is compared with static solutions.

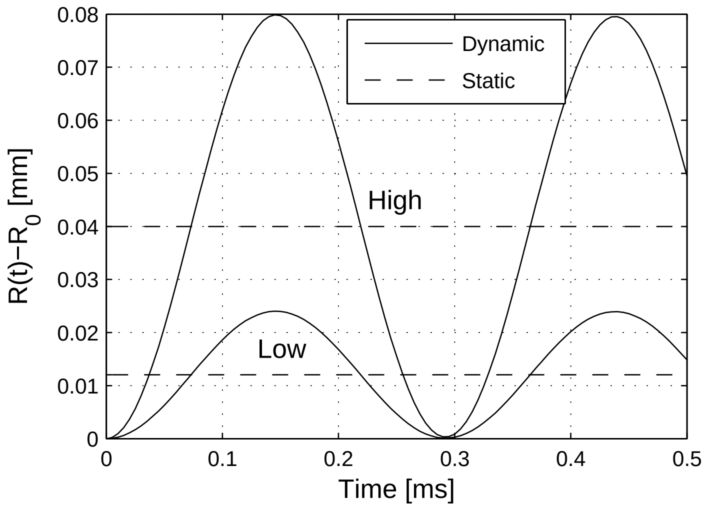

Fig. A1 Expansion tube histories under low and high pressure conditions.

Table A1 compares maximum tube wall radial displacement (max($R(t) - R_0$)) obtained using the analytic dynamic solution with the corresponding values obtained using the FE numerical simulation FE – 3D$_C$. The discrepancy observable in the table is due to the different load histories in the two models (constant pressure for the analytical model and experimental decreasing pressure for the numerical model) and probably also due to a slight overestimation of the modal stiffness of the discretized tube. The results of Table A1 provide a good validation of the FE solid dynamics model.

Test type	Analytical model		FE-3DC model	
	Maximum radial displacement (mm)	Fundamental period (ms)	Maximum radial displacement (mm)	Fundamental period (ms)
Low pressure	2.40×10^{-2}	0.29	1.85×10^{-2}	0.27
High pressure	7.98×10^{-2}	0.29	5.88×10^{-2}	0.27

Table. A1 Maximum expansion tube radial displacement and corresponding fundamental period under low and high pressure conditions.

APPENDIX B

Pressure losses in the shock tube due to the formation of a boundary layer past the shock and the rarefaction wave were investigated in [36-40]. In this Appendix, the simplified model of Mirels [39] and Mirels and Mullen [40] is applied to the present configuration to determine the influence of boundary layer losses on incident peak pressure value.

The model is based on a number of simplifying assumptions, as follows. The governing equations are linearized according to the small perturbation hypothesis, which is valid here provided that the boundary layer is thin with respect to tube diameter. Longitudinal waves are assumed to be one-dimensional and the thickness of the rarefaction wave is assumed to be zero. The latter two assumptions are valid provided that the shock and rarefaction intensity are small. Further details on the method can be found in [39-40].

Figure B1 shows pressure reduction due to the presence of the boundary layer in the less favorable scenario, namely, the high pressure test scenario. As it moves away from the diaphragm location, the post-shock pressure deviates from the (constant) value predicted by the inviscid one-dimensional theory because of viscous losses. Mirels' model, however, predicts that the maximum relative pressure loss due to viscous effects that is observed at the tube end-wall is 2.5% a value that is negligible with respect to all the non-ideal pressure losses discussed in the main text of the paper.

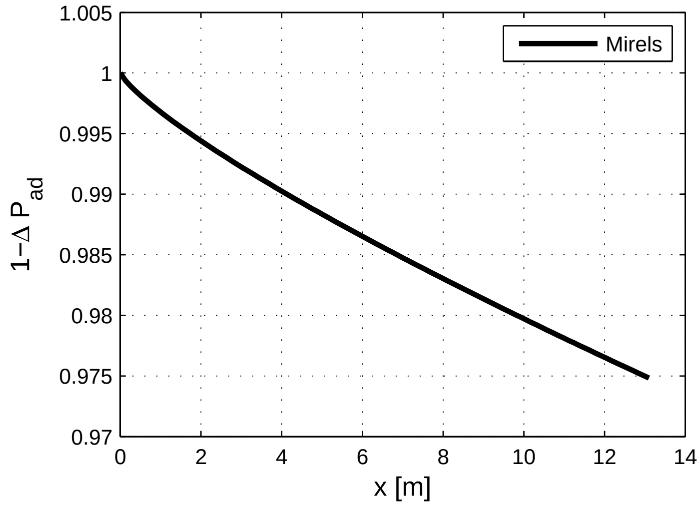

Fig. B1 Pressure reduction due to boundary layer effect in the high pressure scenario. The quantity $1 - \Delta P_{ad}$ is the relative reduction in over-pressure past the shock wave, and it depends on the shock coordinate x, that is, the distance from the diaphragm. The difference $1 - \Delta P_{ad}$ is $(P_{re}-P_{id})/P_{id}$, with P_{re} post-shock pressure according to the Mirels model [39-40] and P_{id} post-shock pressure from the ideal one-dimensional inviscid theory.

REFERENCES

[1] Zhu F, Zhao L, Lu G, Wang Z (2008) Deformation and failure of blast-loaded metallic sandwich panels-experimental investigations. Int J Impact Eng 35:937–951

[2] Carriere M, Heffernan PJ, Wight RG, Braimah A (2009) Behaviour of steel reinforced polymer (SRP) strengthened RC members under blast load. Can J Civil Eng 36:1356–1365

[3] Razaqpur AG, Contestabile E, Tolba A (2009) Experimental study of the strength and deformations of carbon fibre reinforced polymer (CFRP) retrofitted reinforced concrete slabs under blast load. Can J Civil Eng 36:1366–1377

[4] Carey NL, Myers JJ (2010) Full scale blast testing of hybrid barrier systems. ACI Special Publication (281 SP):152–170

[5] Akers SA, Rickman DD, Ehrgott JQ, Shelton TW (2010) Explosive breaching of reinforced concrete walls: Experimental efforts and numerical simulations. ACI Special Publication (281 SP):249–261

[6] Tanapornraweekit G, Haritos N, Mendis P (2011) Behavior of FRP-RC slabs under multiple independent air blasts. J Perform Constr Fac 25:433–440

[7] Abou-Zeid BM, El-Dakhakhni WW, Razaqpur AG, Foo S (2011) Performance of unreinforced masonry walls retrofitted with externally anchored steel studs under blast loading. J Perform Constr Fac 25:441–453

[8] Naito C, Dinan R, Bewick B (2011) Use of precast concrete walls for blast protection of steel stud construction. J Perform Constr Fac 25:454–463

[9] Wu C, Huang L, Oehlers DJ (2011) Blast testing of aluminum foam-protected reinforced concrete slabs. J Perform Constr Fac 25:464–474

[10] Bonalumi P, Colombo M, di Prisco M (2011) Internal explosions in embedded concrete pipes, App. Mech. Mater. 82:452–457

[11] Duong DH, Hanus JL, Bouazaoui L, Pennetier O, Moriceau J, Prod'Homme G, Reimeringer M (2012) Response of a tank under blast loading - part I: Experimental characterisation of blast loading arising from a gas explosion. Eur J Environ Civ En 16:1023–1041

[12] Lloyd A, Jacques E, Saatcioglu M, Palermo D, Nistor I, Tikka T (2010) Capabilities of a shock tube to simulate blast loading on structures. ACI Special Publication (281 SP):35–54

[13] Culbertson DW (1967) A description and predicted performance of a conical shock tube nuclear-blast simulator. 1st Int. Symp. on Military Applications of Blast Simulators (MABS 1), Alberta, Canada

[14] Andrews EH, Bernstein L, Nurse PJ, Reed PE (1971) Impact testing of plastics using a shock tube. In: Eight Int. Symp on Shock Tube, London, 60/1-60/12

[15] Leys IC (1983) AWRE Foulness nuclear air blast simulator: construction and calibration of the enlarged facility. 8th Int. Symp. on Military Applications of Blast Simulation (MABS 8), Spiez, Switzerland

[16] Ritzel DV, Thibault PA (1987) Development of an efficient low-cost blast tube facility. Proc. Tenth Int. Symp. on Military Applications of Blast Simulation (MABS 10), Freiburg, Germany

[17] Ritzel DV, et al., Editors (1995) Nuclear Blast and Thermal Test Methods and Procedures, Edition 1, NATO Allied Engineering Publication, AEP-25

[18] Toutlemonde F, Boulay C, Gourraud C (1993) Shock-tube tests of concrete slabs. Mater Struct 26:38–42

[19] Toutlemonde F, Rossi P, Boulay C et al (1995) Dynamic behavior of concrete –tests of slabs with a shock-tube. Mater Struct 28:293–298

[20] Stoffel M, Schmidt R, Weichert D (2001) Shock wave-loaded plates. Int J Impact Eng 38:7659–7680

[21] Mayrhofer C (2001) Reinforced masonry walls under blast loading. Int J Mech Sci 44:1067-1080

[22] Hernandez-Gomez LH, Ruiz C (1993) Assessment of data for dynamic crack initiation under shock pressure loading: Part I-experiment. Theor Appl Fract Mec 19:75–83

[23] Leblanc J, Shukla A, Rousseau C et al (2007) Shock loading of three-dimensional woven composite materials. Compos Struct 79:344–355

[24] Ritzel D., Scherbatiuk K, Parks SA (2009) A large blast simulator for structural testing. Proceedings of the 8th International Conference on Shock and Impact Loads on Structures, 537-544

[25] Colombo M, di Prisco M, Martinelli P (2011) A new shock tube facility for tunnel safety. Exp Mech 51:1143–1154

[26] Hebert M, Rousseau CE, Shukla A (2008) Shock loading and drop weight impact response of glass reinforced polymer composites. Compos Struct 84:199–208

[27] Colombo M, di Prisco M, Martinelli P (2013) Layered high performance concrete plates interacting with granular soil under blast loads: an experimental investigation. Eur J Environ Civ En 17: 1002–1025

[28] Tang S (1963) Dynamic response of a thin-walled cylindrical tube under internal moving pressure. PhD Thesis discussed at University of Michigan

[29] Beltman WM, Burcsu EN, Shepherd JE, Zuhal L (1999) The Structural response of Cyclindrical Shells to Internal Shock Loading. Journal of Pressure Vessel Technology 121:315–322

[30] Sperber A, Schildberg HP, Schlehlein S (1999) Dynamic load on a pipe caused by acetylene detonations - experiments and theoretical approaches. Shock and Vibration 6:29–43

[31] Beltman WM, Shepherd JE (2002) Linear elastic response of tubes to internal detonation loading. Journal of Sound and Vibration 252:617–655

[32] Mirzaei M, Biglari H, Salavatian M (2006) Analytical and numerical modeling of the transient elasto-dynamic response of a cylindrical tube to internal gaseous detonation. International Journal of Pressure Vessels and Piping 83:531–539

[33] Szirti D, Loiseau J, Higgins A, Tanguay V (2011) Dynamics of explosively imploded pressurized tubes. J Appl Phys 109:084526

[34] Minwei G (2006) Mutual Interactions between shock Waves and Structures. PhD Thesis discussed at City University of New York

[35] Dong Q, Li QM, Zheng JY (2010) Interactive mechanisms between the internal blast loading and the dynamic elastic response of spherical containment vessels. International Journal of Impact Engineering 37:349–358

[36] Donaldson C, Sullivan RD (1949) The Effect of Wall Friction on the Strength of Shock Waves in Tubes and Hydraulic Jumps in Channels. NACA TN 1942

[37] Glass II, Patterson GN (1955) A theoretical and experimental study of shock-tube flows. Jour Aero Sci 22

[38] Hollyer RN (1953) A study of Attenuation in the Shock Tube. Eng. Res. Inst., University of Michigan

[39] Mirels H (1963) Test time in low-pressure shock tubes. Phys Fluids 6:1201–1214

[40] Mirels H, Mullen JF (1964) Small perturbation theory for shock-tube attenuation and nonuniformity. Phys Fluids 7:1208–1218

[41] Alpher RA, White DR (1958) Flow in shock tube with area change at the diaphragm section. J Fluid Mech 3:457–470

[42] White DR (1958) Influence of diaphragm opening time on shock-tube flows. J Fluid Mech 4:585–599

[43] Rothkopf EM, Low W (1974) Diaphragm opening process in shock tubes. Phys Fluids 17:1169–1173

[44] Petrie-Repar P, Jacobs PA (1998) A computational study of shock speeds in high-performance shock tubes. Shock Waves 8:79–91

[45] Persico G, Gaetani P, Guardone A (2005) Dynamic calibration of fast-response probes in low-pressure shock tubes. Meas Sci Technol 16:1751–1759

[46] Gaetani P, Guardone A, Persico G (2008) Shock tube flows past partially opened diaphragms. J Fluid Mech 602:267–286

[47] Tretjakovas J, Kačianauskas R, Šimkevičius Č (2006) FE simulation of rupture of diaphragm with initiated defect, Mechanika 6 :1392–1207

[48] Colombo M, Martinelli P, di Prisco M (2014) Validation of a Computational Approach to Predict Bursting Pressure of Scored Steel Plates. Exp Mech 54:1555–1573

[49] UNI EN 10025-2 (2005) Hot rolled products of structural steels Part 2: Technical delivery conditions for non-alloy structural steels. European Committee for Standardization, Brussels, Belgium

[50] LeVeque RJ. Finite-Volume Methods for Hyperbolic Problems. Cambridge University Press; 2002

[51] LS–DYNA (2003) Version 971 User’s Manual, Livermore Software Technology Corporation

[52] UNI EN ISO 6892-1 (2009) Metallic materials - Tensile testing - Part 1: Method of test at room temperature. European Committee for Standardization, Bruxelles, Belgium